

Apparent double- T_c from a single BKT transition in anisotropic phase-only models

Pei-Yuan Cai^{1,2} and Yi Zhou^{1,*}

¹*Institute of Physics, Chinese Academy of Sciences, Beijing 100190, China*

²*School of Physical Sciences, University of Chinese Academy of Sciences, Beijing 100190, China*

(Dated: May 12, 2026)

Transport experiments on two-dimensional superconductors often yield direction-dependent transition temperatures, raising the question of whether such a “double- T_c ” reflects a true thermodynamic splitting or a transport artifact. To establish a baseline, we study a minimal anisotropic phase-only Josephson-junction array in equilibrium and under resistively shunted junction dynamics with fluctuating twist boundary conditions. The equilibrium model exhibits a single Berezinskii–Kosterlitz–Thouless (BKT) transition. Out of equilibrium, anisotropic Josephson couplings and anisotropic dissipation reshape the linear R – T curves in a finite-size, finite-current crossover regime, so that curve-shape criteria such as Halperin–Nelson fits and fixed-resistance thresholds yield an apparent double- T_c . In contrast, critical-scaling criteria—the universal exponent $\alpha = 3$ and dynamic finite-size scaling—remain consistent with the single T_{BKT} . A robust splitting that persists in the non-linear critical scaling, such as that recently reported at KTaO_3 interfaces, therefore points to physics beyond this clean anisotropic baseline.

I. INTRODUCTION

In two-dimensional (2D) superconductors, phase coherence is governed not merely by the mean-field onset of the order-parameter amplitude, but predominantly by phase fluctuations and topological defects. In the standard Berezinskii–Kosterlitz–Thouless (BKT) paradigm, the true thermodynamic transition is driven by the unbinding of integer vortex–antivortex pairs, marked by a universal jump in the renormalized superfluid stiffness (or helicity modulus) [1–6]. Experimentally, however, the thermodynamic transition must be inferred from nonequilibrium transport measurements, typically manifesting as nonlinear current–voltage (I – V) characteristics and a rapid drop in linear resistance–temperature (R – T) curves [7–9]. Because finite sample sizes and probe currents inherently cut off critical divergences, transport-extracted temperatures obtained from these operational metrics are not automatically identical to the underlying equilibrium BKT temperature T_{BKT} .

This distinction between thermodynamics and transport becomes paramount when the macroscopic response is strongly direction-dependent. Recent transport experiments on oxide heterointerfaces, specifically $\text{EuO}/\text{KTaO}_3(110)$ and (111) , have brought this issue into sharp focus [10, 11]. In these systems, the superconducting transition temperature and upper critical fields depend distinctly on the in-plane current direction. Interpretations of such an apparent “double- T_c ” often invoke exotic, spatially segregated physics, such as quasi-one-dimensional superconducting stripes where phase coherence develops earlier along one crystallographic axis than another. The fundamental question is therefore: does a direction-dependent transport-extracted temperature necessarily imply a split thermodynamic transition (or exotic spatially decoupled phases), or can it emerge as a transport artifact in a system with a single, uniform BKT transition?

Recently, several theoretical frameworks have been pro-

posed to explain this striking experimental phenomenon. For instance, Li, Kivelson, and Lee demonstrated that an infinitely anisotropic superconducting phase can emerge via the unbinding of half-vortices [12]. Concurrently, Xu, Jiang, and Hu highlighted the critical role of anisotropic vortex motion induced by asymmetric pinning landscapes [13]. These sophisticated models provide compelling mechanisms for true directional decoupling. However, they also motivate a foundational theoretical question: before invoking higher-order topological defects or explicit disorder potentials, what is the baseline expectation? Specifically, how much of the apparent double- T_c phenomenology naturally arises from the simplest clean, anisotropic phase-only model?

In this work, we address this by studying a coarse-grained anisotropic Josephson-junction array (JJA) in both equilibrium and nonequilibrium settings. In equilibrium, the model reduces to an anisotropic XY model, and the true thermodynamic transition is determined from the helicity modulus. Out of equilibrium, we evolve the same phase-only Hamiltonian using resistively shunted junction dynamics (RSJD) under fluctuating twist boundary conditions (FTBC) [14–18]. This unified approach allows us to separate the equilibrium BKT temperature from the criterion-dependent transport-extracted temperatures obtained from finite-current E – j and r_{lin} – T curves, as the numerical counterparts of experimental I – V and R – T transport measurements.

Our results demonstrate that a purely continuous anisotropic model supports only a single thermodynamic BKT transition, dictated by the geometric mean of the directional stiffnesses. However, finite-current r_{lin} – T curves can readily display an apparent, direction-dependent splitting of transport-extracted temperatures. We show that this splitting is not a thermodynamic reality, but a crossover effect. Because finite system sizes and probe currents truncate the critical divergence of the correlation length, R – T curve fits (such as the Halperin–Nelson formula) are forced into a higher-temperature crossover regime. In this regime, non-universal anisotropic Josephson couplings and anisotropic dissipation—which phenomenologically captures anisotropic viscous vortex drag—reshape the resistive curves differently

* yizhou@iphy.ac.cn

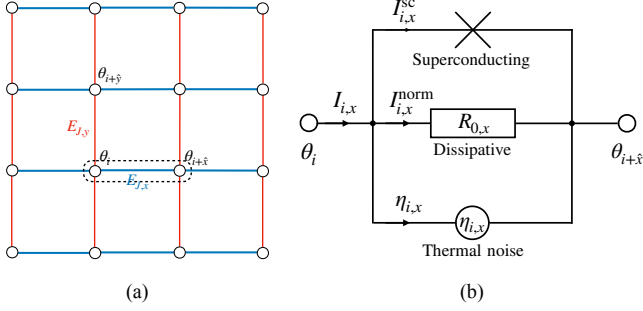


FIG. 1. Schematic of the anisotropic phase-only model and the RSJ dynamics. (a) Coarse-grained anisotropic JJA/XY model on a square lattice. The superconducting phase on site i is denoted by θ_i . Horizontal and vertical bonds represent the effective Josephson stiffnesses $E_{J,x} = qE_*$ and $E_{J,y} = (1-q)E_*$, respectively. (b) RSJ representation example of the boxed x -directed bond in (a). The total bond current $I_{i,x}$ is decomposed into three channels given in Eq. (22). The corresponding y -bond is obtained by replacing x with y .

along orthogonal axes, leading curve-shape criteria to yield two distinct apparent transport-extracted temperatures.

Crucially, we find that criteria tied directly to critical transport scaling are much less sensitive to this crossover artifact. The nonlinear I - V exponent criterion ($\alpha = 3$) and dynamic finite-size scaling (FSS) are less affected by the curve-reshaping and remain consistent with the single equilibrium BKT temperature T_{BKT} . By contrasting the failure of R - T fits with the robustness of I - V scaling, our model provides a useful diagnostic comparison for experimentalists. In the scenario captured by the present clean baseline, an apparent directional splitting in the transport-extracted temperatures from R - T curves is not accompanied by a resolvable splitting in the critical scaling criteria. Conversely, if the splitting persists in the $\alpha = 3$ critical scaling—as is notably the case in recent EuO/KTaO₃(111) measurements [11]—it suggests that the system harbors exotic physics beyond the standard continuous anisotropic BKT paradigm.

The rest of the paper is organized as follows. Section II introduces the anisotropic JJA model and the observables used in the equilibrium and nonequilibrium analyses. Section III presents the numerical results, contrasting the single thermodynamic transition with the bifurcated transport extractions. Section IV summarizes the physical picture, discusses the mechanism of anisotropic curve reshaping, and outlines the scope and application of this theoretical baseline.

II. MODEL AND NUMERICAL OBSERVABLES

A. Effective anisotropic JJA model

We consider a two-dimensional superconducting order parameter

$$\Psi(\mathbf{r}) = |\Psi(\mathbf{r})|e^{i\theta(\mathbf{r})}, \quad \mathbf{r} = (x, y).$$

In the temperature window of interest, namely below the mean-field pairing scale T_{MF} and near the BKT transition, amplitude fluctuations are assumed to be less important than phase fluctuations. The long-wavelength free energy is then approximated by the phase-only form

$$F[\theta] = \frac{1}{2} \int d^2\mathbf{r} \sum_{\mu=x,y} \rho_{\mu} (\partial_{\mu}\theta)^2,$$

where ρ_{μ} is the phase stiffness along direction μ .

After coarse graining onto an $L \times L$ lattice of superconducting islands [see Fig. 1(a)], we denote the phase on site i by θ_i and write the effective Hamiltonian as

$$H = - \sum_i \sum_{\mu=x,y} E_{J,\mu} \cos \phi_{i,\mu}, \quad (1)$$

with the gauge-invariant phase difference

$$\phi_{i,\mu} = \theta_{i+\hat{\mu}} - \theta_i + A_{i,\mu}. \quad (2)$$

For a literal Josephson-junction array, $E_{J,\mu} = \hbar I_{c,\mu} / (2e)$ is the Josephson coupling energy of a junction. In the present coarse-grained description of a continuous two-dimensional superconductor, $E_{J,\mu}$ should be viewed more generally as an effective bond stiffness. It is the local energy cost of twisting the superconducting phase across a coarse-grained bond in direction μ .

For the zero-field problem studied here, the link twist $A_{i,\mu}$ is introduced only to encode a boundary twist. A total twist Θ_{μ} along direction μ may be represented either by a uniform link twist $A_{i,\mu} = A_{\mu} = \Theta_{\mu} / L$ with periodic boundary conditions (PBC) on θ_i , or equivalently by gauging away A_{μ} and imposing twisted boundary conditions (TBC) on the phase variables. The two descriptions are gauge equivalent and lead to the same equilibrium thermodynamics.

To parameterize the anisotropy, throughout this work we use:

$$E_{J,x} = qE_*, \quad E_{J,y} = (1-q)E_*, \quad \frac{1}{2} \leq q < 1, \quad (3)$$

where $E_* = E_{J,x} + E_{J,y}$ sets the overall energy scale. With $k_B = 1$, temperature is measured in the same units. We exclude $q = 1$ because the system turns into one-dimensional chains there and no finite-temperature BKT transition remains. The isotropic limit corresponds to $q = 1/2$, for which Eq. (1) becomes

$$H = -\frac{E_*}{2} \sum_i (\cos \phi_{i,x} + \cos \phi_{i,y}).$$

Comparison with the standard isotropic XY Hamiltonian $H = -J \sum_i (\cos \phi_{i,x} + \cos \phi_{i,y})$ shows that the isotropic coupling is $J = E_*/2$. Thus, if one sets $E_* = 1$, the isotropic transition temperature is $T_{\text{BKT}} \approx 0.446$, i.e., one half of the usual unit-coupling value ≈ 0.893 [19–22].

The model in Eq. (1) provides the common starting point for our analysis. In the classical equilibrium limit, it is equivalent to the two-dimensional anisotropic XY model [23–25]. Out of equilibrium, the nonlinear transport can be studied by the RSJD, which governs the phase evolution under external driving currents and thermal fluctuations [14–18].

B. Equilibrium: universal jump and helicity modulus

1. Single BKT transition from the long-wavelength theory

The equilibrium question is whether anisotropy can split the BKT transition into two distinct transitions. To address this, we expand Eq. (1) for smoothly varying phase configurations with $A_{i,\mu} = 0$. The spin-wave part of the dimensionless energy is

$$\frac{F_{\text{sw}}}{T} = \frac{1}{2} \int d^2\mathbf{r} [K_x(\partial_x\theta)^2 + K_y(\partial_y\theta)^2], \quad (4)$$

where

$$K_x = \frac{E_{J,x}}{T}, \quad K_y = \frac{E_{J,y}}{T} \quad (5)$$

are the bare dimensionless stiffnesses.

The anisotropy can be removed by the coordinate rescaling

$$x' = \left(\frac{K_y}{K_x}\right)^{1/4} x, \quad y' = \left(\frac{K_x}{K_y}\right)^{1/4} y, \quad (6)$$

which transforms Eq. (4) into

$$\frac{F_{\text{sw}}}{T} = \frac{\bar{K}_0}{2} \int d^2\mathbf{r}' (\nabla'\theta)^2, \quad (7)$$

with the effective bare stiffness

$$\bar{K}_0 = \sqrt{K_x K_y} = \frac{\sqrt{E_{J,x} E_{J,y}}}{T}. \quad (8)$$

The long-wavelength theory therefore depends on the anisotropy only through the geometric mean $\sqrt{K_x K_y}$. The standard BKT renormalization-group flow[2–4, 26] then applies with $K \rightarrow \bar{K}$:

$$\frac{d\bar{K}^{-1}}{dl} = 4\pi^3 y^2 + \mathcal{O}(y^4), \quad (9)$$

$$\frac{dy}{dl} = (2 - \pi\bar{K})y + \mathcal{O}(y^3), \quad (10)$$

where y is the vortex fugacity. Along the critical trajectory, the renormalized stiffness approaches the fixed point[4]

$$\bar{K}_R(T_{\text{BKT}}^-) = \frac{2}{\pi}. \quad (11)$$

Equivalently, in terms of the renormalized effective helicity modulus

$$\bar{\Upsilon}_R \equiv T\bar{K}_R, \quad (12)$$

one obtains the Nelson–Kosterlitz jump condition at the BKT transition temperature[21, 24, 25]

$$\bar{\Upsilon}_R(T_{\text{BKT}}^-) = \frac{2T_{\text{BKT}}}{\pi}. \quad (13)$$

Thus the anisotropy changes the stiffness scale, but the BKT transition is still controlled by a single critical temperature.

2. Directional helicity modulus

In the numerical simulations we evaluate the directional helicity moduli, which are defined by

$$\Upsilon_\mu(L, T) \equiv \left. \frac{\partial^2 F}{\partial \Phi_\mu^2} \right|_{\Phi_\mu=0}, \quad (14)$$

as the free-energy response to an infinitesimal extra boundary twist Φ_μ along the μ direction[5, 24, 25] under given system size L , temperature T and most importantly, under PBC, i.e., $\Theta_\mu = 0$. It is convenient to introduce the twist per bond

$$\delta_\mu \equiv \Phi_\mu/L, \quad (15)$$

so that

$$\Upsilon_\mu(L, T) = \frac{1}{L^2} \left. \frac{\partial^2 F}{\partial \delta_\mu^2} \right|_{\delta_\mu=0}. \quad (16)$$

For the Hamiltonian in Eq. (1), this gives

$$\Upsilon_\mu(L, T) = \frac{1}{L^2} \langle C_\mu \rangle - \frac{\beta}{L^2} [\langle S_\mu^2 \rangle - \langle S_\mu \rangle^2], \quad (17)$$

where

$$S_\mu \equiv \sum_i E_{J,\mu} \sin \phi_{i,\mu}, \quad C_\mu \equiv \sum_i E_{J,\mu} \cos \phi_{i,\mu}.$$

Here the gauge-invariant phase difference becomes $\phi_{i,\mu} = \theta_{i+\hat{\mu}} - \theta_i$ under $A_\mu = \Theta_\mu/L = 0$. The detailed derivation of Eq. (17) is given in Appendix A.

The quantity entering the equilibrium BKT criterion is the geometric mean

$$\tilde{\Upsilon}(L, T) \equiv \sqrt{\Upsilon_x(L, T)\Upsilon_y(L, T)}. \quad (18)$$

For each system size L , we define $T^*(L)$ by the crossing

$$\tilde{\Upsilon}(L, T) = \frac{2T}{\pi}, \quad (19)$$

and estimate the equilibrium BKT temperature from the finite-size form

$$T^*(L) = T_{\text{BKT}} + \frac{A}{\ln^2(bL)}, \quad (20)$$

with A and b fitting parameters [19–21, 27]. In the present work, T_{BKT} is referred to as the equilibrium BKT temperature, namely our finite-size estimate of the thermodynamic BKT transition temperature.

We emphasize that the helicity modulus (Eq. (14)) is defined under zero boundary twist. Accordingly, the BKT criterion in Eq. (13) and the finite-size form in Eq. (20) are applied only to the system under zero boundary twist. At a finite boundary twist, one may instead define a finite-twist stiffness response at $\Theta_\mu \neq 0$. This quantity is not identical to Eq. (14) and is not used to determine T_{BKT} . Throughout the equilibrium analysis the boundary twist is fixed at zero, and finite-twist consistency checks (which require a modified cluster update) are presented in Appendix A 2.

C. Nonequilibrium dynamics: RSJD under FTBC

1. Equations of motion

To study finite-current transport, we evolve the same phase-only model with RSJD under FTBC [14–18, 28]. In FTBC the local phases remain periodic,

$$\theta_{i+L\hat{x}} = \theta_i, \quad \theta_{i+L\hat{y}} = \theta_i,$$

while the uniform twist variables Δ_μ are absorbed into the bond phase differences,

$$\phi_{i,\mu} = \theta_{i+\hat{\mu}} - \theta_i - \Delta_\mu. \quad (21)$$

The ‘‘fluctuating twist’’ means that Δ_μ will also be evolved in every time step when solving the Langevin equations.

The resistively shunted junction interpretation of a single bond is shown in Fig. 1(b). On each bond, the total current is written as[29, 30]

$$I_{i,\mu} = I_{i,\mu}^{\text{sc}} + I_{i,\mu}^{\text{norm}} + \eta_{i,\mu}. \quad (22)$$

The three terms are interpreted as follows.

1. *Superconducting channel.* Following the current-phase relation of a Josephson junction[31], the superconducting current is given by

$$I_{i,\mu}^{\text{sc}} = \frac{2e}{\hbar} \frac{\partial}{\partial \phi_{i,\mu}} (-E_{J,\mu} \cos \phi_{i,\mu}) = I_{c,\mu} \sin \phi_{i,\mu}, \quad (23)$$

with $I_{c,\mu} = (2e/\hbar)E_{J,\mu}$.

2. *Dissipative channel.* The voltage across a bond is related to the phase by the Josephson relation, $V_{i,\mu} = (\hbar/2e)\dot{\phi}_{i,\mu}$. The dissipative current is modeled as an Ohmic shunt,

$$I_{i,\mu}^{\text{norm}} = \frac{V_{i,\mu}}{R_{0,\mu}} = \frac{\hbar}{2eR_{0,\mu}} \dot{\phi}_{i,\mu}, \quad (24)$$

where $R_{0,\mu}$ is the coarse-grained bond shunt resistance along direction μ .

3. *Thermal noise channel.* Following the Langevin formalism introduced by Ambegaokar and Halperin [32], the noise current satisfies the fluctuation–dissipation theorem,

$$\langle \eta_{i,\mu}(t) \rangle = 0, \quad (25)$$

$$\langle \eta_{i,\mu}(t) \eta_{j,\nu}(t') \rangle = \frac{2k_B T^{\text{phys}}}{R_{0,\mu}} \delta_{ij} \delta_{\mu\nu} \delta(t - t'). \quad (26)$$

The equations of motion follow from Kirchhoff current conservation at every site together with the condition that the spatially averaged current equals the applied current density[15, 28–30, 32]. Their derivation is summarized in Appendix B. After introducing the dimensionless variables defined there,

we can obtain the equations of motion for the phase and twist variables:

$$\dot{\theta}_i = \sum_j G_{ij}^{(r_0)} \sum_{\mu=x,y} [\mathcal{J}_{j,\mu}^{\text{sc}} - \mathcal{J}_{j-\hat{\mu},\mu}^{\text{sc}} + \zeta_{j,\mu} - \zeta_{j-\hat{\mu},\mu}], \quad (27)$$

$$\dot{\Delta}_\mu = r_{0,\mu} \left[\frac{1}{L^2} \sum_i \mathcal{J}_{i,\mu}^{\text{sc}} + \zeta_{\Delta_\mu} - j_\mu \right], \quad \mu = x, y, \quad (28)$$

where the dot denotes differentiation with respect to dimensionless time τ , and $G_{ij}^{(r_0)}$ is the lattice Green’s function of the weighted discrete Laplacian. The dimensionless superconducting current is given by

$$\mathcal{J}_{i,\mu}^{\text{sc}} = J_\mu \sin \phi_{i,\mu}, \quad J_\mu \equiv \frac{E_{J,\mu}}{E_*}, \quad (29)$$

and the dimensionless shunt resistance $r_{0,\mu}$ and spatially averaged noise current ζ_{Δ_μ} are:

$$r_{0,\mu} \equiv \frac{R_{0,\mu}}{R_*}, \quad \zeta_{\Delta_\mu} \equiv \frac{1}{L^2} \sum_i \zeta_{i,\mu}. \quad (30)$$

The dimensionless noise satisfies

$$\langle \zeta_{i,\mu}(\tau) \zeta_{j,\nu}(\tau') \rangle = \frac{2T}{r_{0,\mu}} \delta_{ij} \delta_{\mu\nu} \delta(\tau - \tau'), \quad (31)$$

$$\langle \zeta_{\Delta_\mu}(\tau) \zeta_{\Delta_\nu}(\tau') \rangle = \frac{2T}{r_{0,\mu} L^2} \delta_{\mu\nu} \delta(\tau - \tau'). \quad (32)$$

The macroscopic voltage drop along direction μ follows from the Josephson relation, and the corresponding electric field is given by:

$$V_\mu = -\frac{\hbar L}{2e} \dot{\Delta}_\mu, \quad E_\mu^{\text{phys}} = -\frac{\hbar}{2e} \dot{\Delta}_\mu, \quad (33)$$

so that the dimensionless electric field measured in the simulation is the long-time average of $\dot{\Delta}_\mu$:

$$E_\mu = -\langle \dot{\Delta}_\mu \rangle_\tau. \quad (34)$$

These equations provide the basis for all transport calculations below.

Throughout the paper, we use $E-j$ and $r_{\text{lin}}-T$ for the dimensionless quantities computed in the simulations. We also refer to them as the numerical counterparts of current–voltage ($I-V$) and resistance–temperature ($R-T$) measurements, respectively. For a fixed square geometry, V_μ and I_μ differ from E_μ and j_μ only by geometric factors. Therefore the nonlinear exponent, scaling collapse, and extracted temperature scales are unaffected by this change of notation.

III. NUMERICAL SIMULATIONS, RESULTS, AND ANALYSIS

Before presenting the numerical results, we clarify the terminology used for temperature scales. The temperature obtained from the equilibrium helicity-modulus analysis will be

| q | 0.5 | 0.6 | 0.7 | 0.8 | 0.9 |
|------------------|-----------|-----------|-----------|-----------|-----------|
| T_{BKT} | 0.4472(3) | 0.4392(4) | 0.4144(6) | 0.3705(5) | 0.2820(6) |

TABLE I. Equilibrium BKT temperatures T_{BKT} of the anisotropic XY model. The temperatures are obtained from the finite-size extrapolation Eq. (20) using $L = 60, 80, 100, 160,$ and 200 , and are measured in units of E_* . Parentheses denote statistical fitting uncertainties.

called the *equilibrium BKT temperature*. It is our finite-size estimate of the thermodynamic BKT transition temperature of the underlying anisotropic XY model. By contrast, all temperatures obtained from nonequilibrium RSJD transport data will be called *transport-extracted temperatures*. These are criterion-dependent operational quantities, analogous to transition temperatures inferred from experimental I - V or R - T measurements, and need not coincide with the equilibrium BKT temperature in a finite-size, finite-current setting. Within the transport-extracted temperatures, we further distinguish critical-scaling criteria, such as the $\alpha = 3$ criterion and dynamic finite-size scaling, from curve-shape criteria, such as Halperin-Nelson fits and fixed-resistance thresholds.

A. Equilibrium

For equilibrium calculations we simulate Eq. (1) on $L \times L$ lattices with $L = 60, 80, 100, 160,$ and 200 using Wolff cluster updates [33]. We study $q = 0.5, 0.6, 0.7, 0.8,$ and 0.9 .

For each q and L , we compute $\Upsilon_x(L, T)$ and $\Upsilon_y(L, T)$ and form

$$\tilde{\Upsilon}(L, T) = \sqrt{\Upsilon_x(L, T)\Upsilon_y(L, T)}.$$

The size-dependent crossing temperature $T^*(L)$ is obtained from $\tilde{\Upsilon}(L, T)/T = 2/\pi$, and Eq. (20) is then used to fit $T_{\text{BKT}}(q)$. As a quality check of the extrapolation, we also plot $[T^*(L; q) - T_{\text{BKT}}(q)]/A(q)$ versus $\ln^{-2}[b(q)L]$ for different q values and perform linear fits in the inset of Fig. 2. The linearity with slope 1 of this plot confirms the validity of the finite-size form in Eq. (20). The resulting values are listed in Table I.

For the largest size $L = 200$, Fig. 2 shows $\tilde{\Upsilon}/T$ for all q . In each case there is only one crossing with $2/\pi$, consistent with a single BKT transition. The transition temperature decreases as the anisotropy increases, as expected from the reduction of the geometric-mean stiffness.

B. Nonequilibrium

Having determined the equilibrium BKT temperature, we now turn to the criterion-dependent transport-extracted temperatures obtained from RSJD simulations. We first keep the dissipative channel isotropic, $r_{0,x} = r_{0,y} = 1$, so that the transport anisotropy comes only from $E_{J,x} \neq E_{J,y}$. We use $q = 0.6$ as the representative example and then compare with $q = 0.7$. After that, we turn on anisotropy in the dissipative channel.

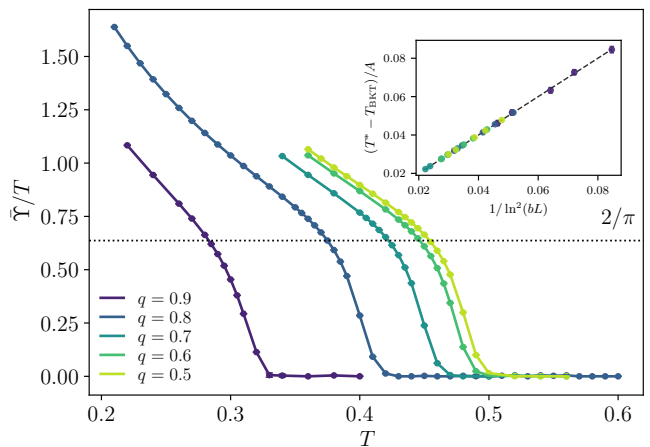


FIG. 2. Geometric-mean helicity modulus divided by temperature, $\tilde{\Upsilon}(L, T)/T$, for $L = 200$. The horizontal dashed line marks the universal jump value $2/\pi$. Each curve crosses $2/\pi$ only once, consistent with a single BKT transition for each q . Inset: the $[T^*(L; q) - T_{\text{BKT}}(q)]/A(q)$ versus $\ln^{-2}[b(q)L]$ data and the corresponding linear fits for different q values as a quality check.

1. Transport criteria: $q = 0.6$ as an example

The nonequilibrium analysis begins from the E - j curves obtained by integrating Eqs. (27) and (28) for currents applied along x and y . The integration is performed by the second-order Runge-Kutta-Helfand-Greenside algorithm for stochastic dynamics[34, 35]. The time step $\Delta\tau$ is set to be 0.02, and the long-time average in Eq. (34) is calculated over $\sim 10^7$ steps for large current densities and $\sim 10^8$ steps for small current densities. Representative data for $L = 100$ and $q = 0.6$ are shown in Fig. 3. Gray points are discarded in the analysis since the signal is dominated by numerical noise.

a. $\alpha = 3$ criterion. A standard way to analyze nonlinear transport near a BKT transition is to define the local slope

$$\alpha_\mu(T, j_\mu) \equiv \frac{d \ln E_\mu}{d \ln j_\mu}. \quad (35)$$

In the ideal Ambegaokar-Halperin-Nelson-Siggia (AHNS) picture[6-8], the transition is identified by $\alpha(T_{\text{BKT}}^-) = 3$. The temperature obtained from this condition will be treated as a critical-scaling transport-extracted temperature.

For the finite anisotropy considered here, this criterion is unchanged by the rescaling used in Sec. II: the stiffness entering AHNS is the renormalized geometric mean $\tilde{\Upsilon}_R$, and a directional E_μ and j_μ acquire only constant metric factors. Thus a power law $E_\mu \propto j_\mu^\alpha$ keeps the same exponent. Since $\alpha(T) = 1 + \pi\tilde{\Upsilon}_R(T)/T$ and $\tilde{\Upsilon}_R(T_{\text{BKT}}^-) = 2T_{\text{BKT}}/\pi$, both directions give $\alpha(T_{\text{BKT}}^-) = 3$.

Figure 4 shows the numerically differentiated α - j data. For both current directions, the $\alpha = 3$ condition falls between $T = 0.44$ and 0.45 , and with the present temperature resolution we take

$$T_x^{\alpha=3} \approx T_y^{\alpha=3} \approx 0.44. \quad (36)$$

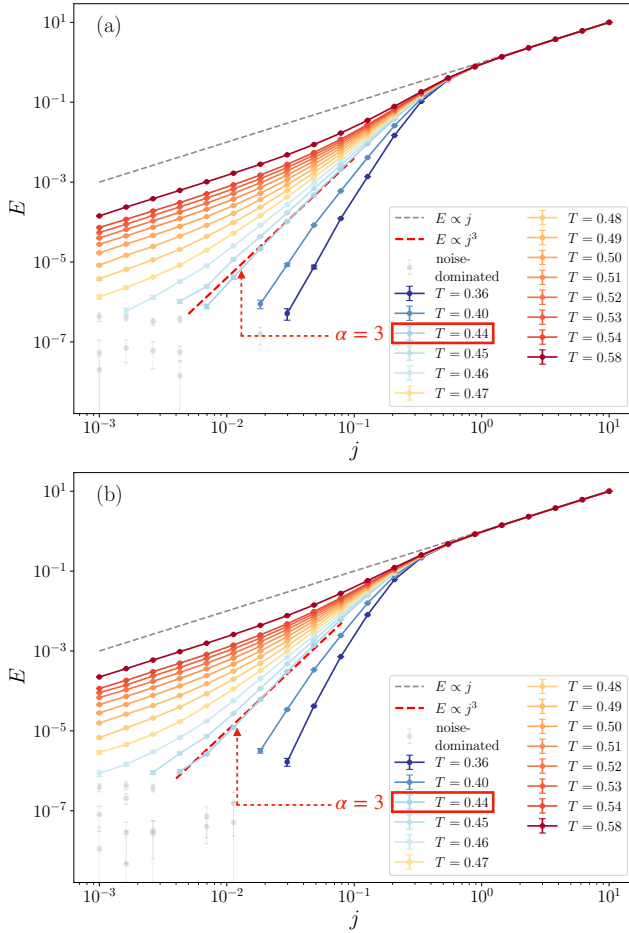


FIG. 3. Dimensionless E - j characteristics for $L = 100$ and $q = 0.6$ with current applied along (a) x and (b) y . The dashed guide lines indicate Ohmic behavior, $E \propto j$, and the BKT critical power law, $E \propto j^3$. Gray data points are dominated by numerical noise and are excluded from the quantitative analysis.

This agrees well with the equilibrium estimate $T_{\text{BKT}} \approx 0.439$ in Table I.

b. Dynamic finite-size scaling. We next examine dynamic finite-size scaling (FSS). In two dimensions, the Fisher–Fisher–Huse form can be written as [16, 36, 37]

$$\frac{E_\mu}{j_\mu} = \xi^{-z} \chi_\pm \left(\frac{j_\mu \xi}{T} \right), \quad (37)$$

where ξ is the correlation length, z is the dynamic critical exponent, and χ_\pm are the scaling functions above and below the BKT transition temperature. In practice, we keep the conventional value $z = 2$ fixed to find the FSS transport-extracted temperature where the data collapse. A finite spatial anisotropy only changes the metric of the correlation lengths, i.e., $\xi_\mu = c_\mu \xi'$. Thus, the relaxation time still scales as $\tau \sim (\xi')^z$ with one exponent. At the transition the divergence of ξ is cut off by the system size, so one expects

$$\frac{E_\mu}{j_\mu} L^z = \chi_\pm \left(\frac{j_\mu L}{T} \right). \quad (38)$$

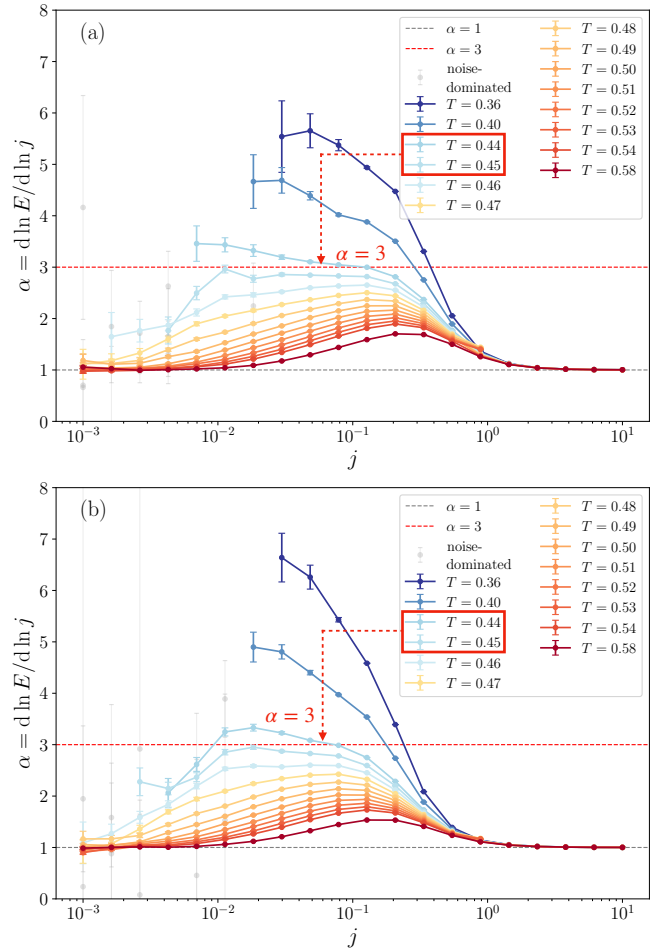


FIG. 4. Local nonlinear transport exponent $\alpha_\mu(T, j_\mu) = (d \ln E_\mu) / (d \ln j_\mu)$ for $L = 100$ and $q = 0.6$, with currents applied along (a) x and (b) y . The horizontal dashed line marks the BKT criterion $\alpha = 3$. The curves from $T = 0.44$ to $T = 0.45$ bracket the crossing for both current directions, consistent with the equilibrium estimate $T_{\text{BKT}} \approx 0.439$.

Using $L = 20, 40, 60, 80,$ and 100 , we plot the finite-size scaling form at $T = 0.44$, the temperature grid point closest to the equilibrium estimate of T_{BKT} , with the conventional dynamic exponent $z = 2$ [16, 37, 38]. As shown in Fig. 5, the same choice of T and z gives comparable collapses for currents driven along x and y :

$$T_x^{\text{FSS}} \approx T_y^{\text{FSS}} \approx 0.44. \quad (39)$$

Like the $\alpha = 3$ criterion, dynamic FSS successfully accounts for the system cutoffs and yields a single critical-scaling transport-extracted temperature for probe currents along both orthogonal directions, and does not indicate a resolvable directional splitting.

c. Linear-response window and $r_{\text{lin}}-T$ curves. To construct an operational linear-resistance curve from the finite-current transport data, one must identify a current window in which the response is approximately Ohmic. We define the

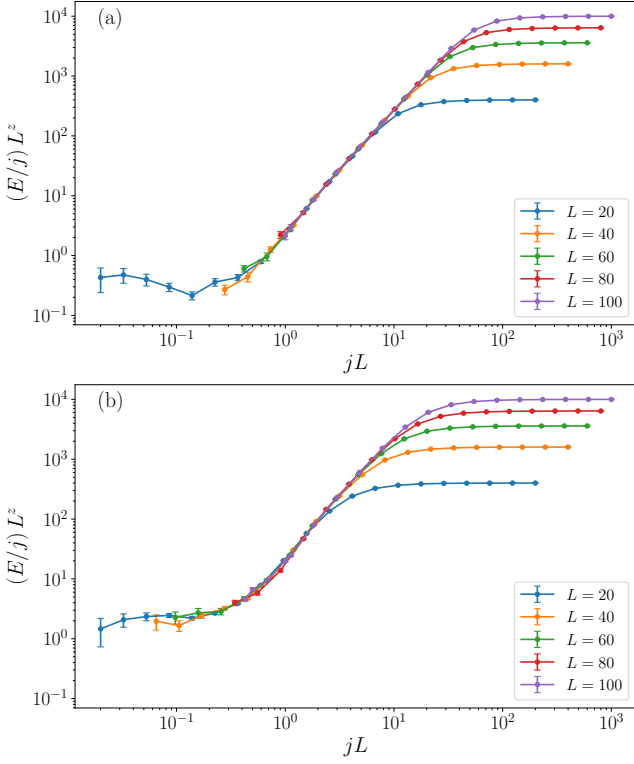


FIG. 5. Dynamic finite-size scaling of the E - j data for $q = 0.6$ at $T = 0.44$. The scaled resistance $(E_\mu/j_\mu)L^z$ is plotted against jL for (a) $j \parallel x$ and (b) $j \parallel y$. System sizes are $L = 20, 40, 60, 80, 100$, and the collapse is obtained with $z = 2$. The same temperature and exponent give comparable collapses for both current directions.

dimensionless resistance at a given probe current as

$$r_{\text{lin},\mu} = \frac{E_\mu}{j_\mu}, \quad (40)$$

for which the low-current response exhibits a plateau consistent with $\alpha_\mu \simeq 1$. In practice, we use $|\alpha_\mu - 1| \leq 0.2$ as the criterion for assigning a data point to the linear-response window[39]. Figure 6 illustrates this for $j = 0.01, 0.005$, and 0.001 .

Choosing an isotropic dissipative channel ($r_{0,x} = r_{0,y} = 1$), the corresponding $r_{\text{lin}}-T$ curves are shown in Fig. 7. We use two empirical threshold criteria common in experimental analysis:

$$\frac{r_{\text{lin},\mu}}{r_{0,\mu}} = 0.5, \quad \frac{r_{\text{lin},\mu}}{r_{0,\mu}} = 0.01, \quad (41)$$

yielding threshold transport-extracted temperatures $T_\mu^{50\%}$ and $T_\mu^{1\%}$, respectively.

For the 50% criterion we obtain

$$\begin{aligned} j = 0.01 : & \quad T_x^{50\%} = 0.808, & T_y^{50\%} = 0.700, \\ j = 0.005 : & \quad T_x^{50\%} = 0.807, & T_y^{50\%} = 0.700, \\ j = 0.001 : & \quad T_x^{50\%} = 0.808, & T_y^{50\%} = 0.701. \end{aligned}$$

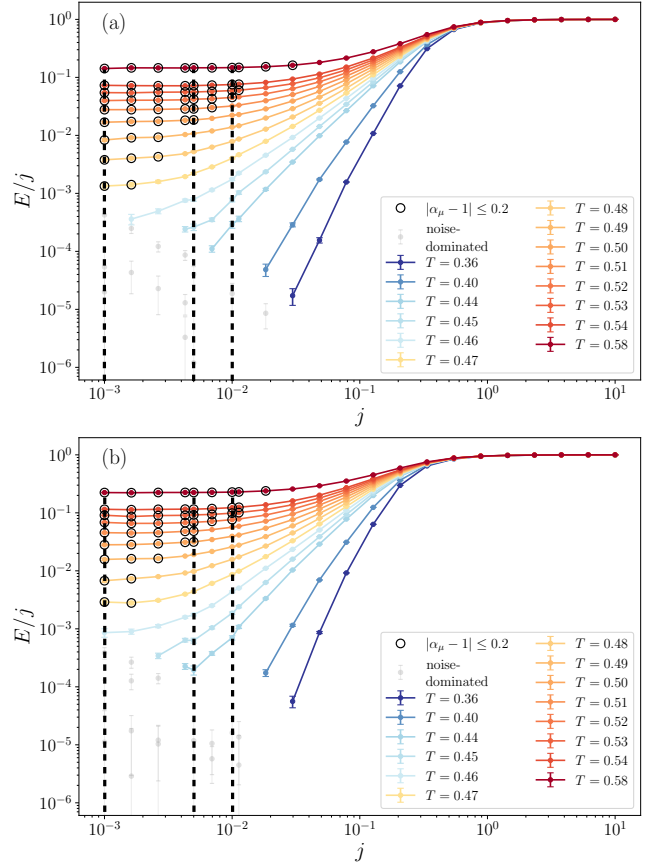


FIG. 6. Linear-response check for the probe currents used to construct $r_{\text{lin},\mu}$. The ratio E_μ/j_μ is plotted as a function of j_μ for $L = 100$ and $q = 0.6$, with current along (a) x and (b) y . The vertical black dashed lines mark $j = 0.01, 0.005$, and 0.001 . Black open circles denote data points retained as linear-response data, selected by the criterion $|\alpha_\mu - 1| \leq 0.2$.

These temperatures are obviously direction dependent, but they are also far above the T_{BKT} . Therefore, $T_\mu^{50\%}$ should be viewed as a threshold transport-extracted temperature that diagnoses the direction-dependent reshaping of the resistive curves, rather than as an estimate of the equilibrium BKT temperature.

A lower resistance threshold moves the extracted temperature closer to T_{BKT} , but only if the intersection still lies inside the linear-response window. Figure 8 shows the relevant low-resistance region. For $j = 0.01$ and 0.005 , the 1% threshold is reached only below the lowest temperature at which the probe current remains linear, so no reliable $T_\mu^{1\%}$ can be assigned. For $j = 0.001$, we can extract

$$T_x^{1\%} = 0.492, \quad T_y^{1\%} = 0.484.$$

Compared with $T_\mu^{50\%}$, these values are much closer to T_{BKT} , and they show a small directional splitting. As the temperature is lowered, $r_{\text{lin},x}$ obtained from the x -direction with larger $E_{J,x}$ will drop below the 1% threshold earlier than the y -direction, giving $T_x^{1\%} > T_y^{1\%}$.

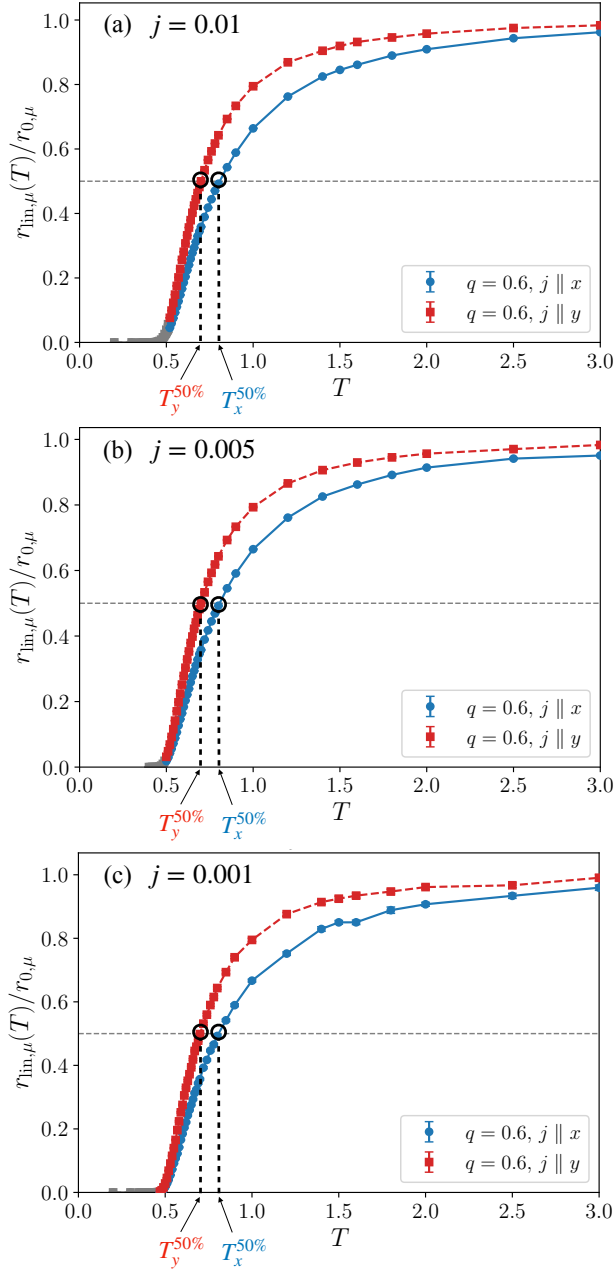


FIG. 7. Normalized linear resistance $r_{\text{lin},\mu}/r_{0,\mu}$ for $L = 100$ and $q = 0.6$ with isotropic dissipation $r_{0,x} = r_{0,y} = 1$ at probe currents (a) $j = 0.01$, (b) $j = 0.005$, and (c) $j = 0.001$. Blue circles and red squares denote currents applied along x and y , respectively. The horizontal dashed line marks the empirical 50% threshold, $r_{\text{lin},\mu}/r_{0,\mu} = 0.5$. Gray points are outside the verified linear-response window and are not used for extracting threshold temperatures.

d. Halperin–Nelson fits. Finally, we fit the linear resistance above the transition to the Halperin–Nelson form [9],

$$r_{\text{lin},\mu}(T) = r_{\mu}^{\text{HN},0} \exp \left[-b_{\mu} \left(\frac{T_{\mu}^{\text{HN}}}{T - T_{\mu}^{\text{HN}}} \right)^{1/2} \right]. \quad (42)$$

Again, the fit is performed only on points inside the linear regime. Representative fits are shown in Fig. 9. We emphasize

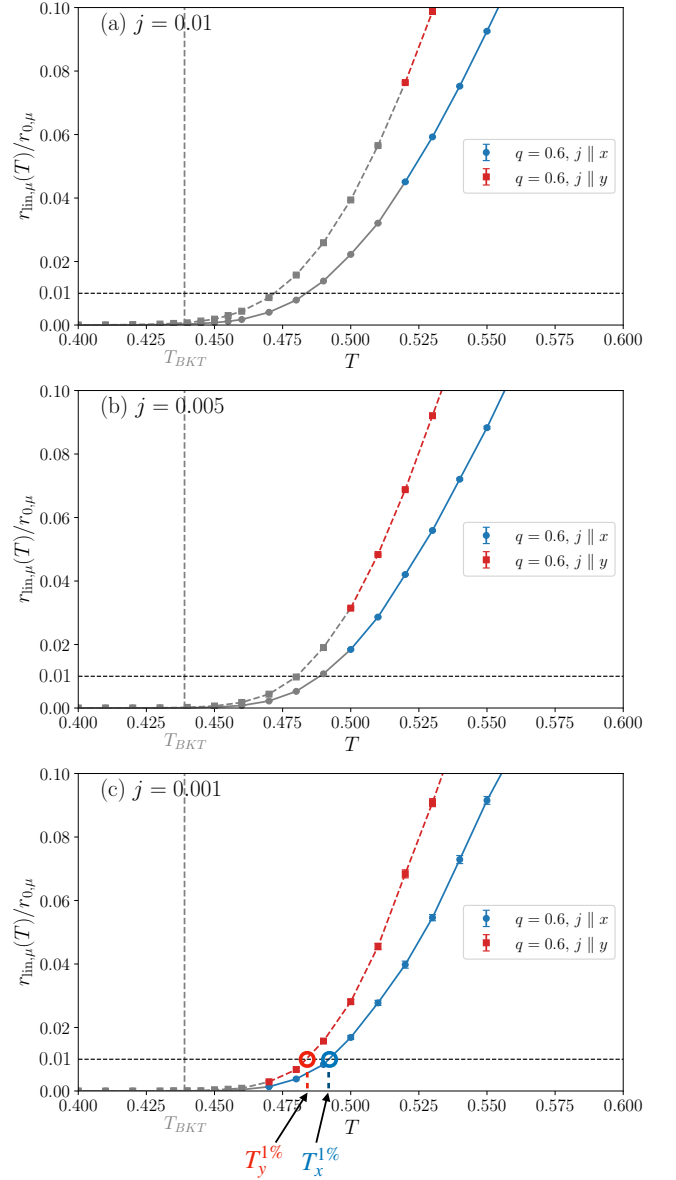


FIG. 8. Zoom-in of low-resistance regions of the normalized linear resistance $r_{\text{lin},\mu}/r_{0,\mu}$ for $L = 100$, $q = 0.6$, and isotropic dissipation $r_{0,x} = r_{0,y} = 1$ at (a) $j = 0.01$, (b) $j = 0.005$, and (c) $j = 0.001$. The horizontal dashed line marks the 1% threshold $r_{\text{lin},\mu}/r_{0,\mu} = 0.01$. The vertical dashed line indicates the equilibrium $T_{\text{BKT}} \approx 0.439$. Gray points lie outside the verified linear-response window and are not used for extracting threshold temperatures.

that T_{μ}^{HN} is used here as an HN transport-extracted temperature obtained from a finite-size, finite-current resistance curve, rather than as an independent estimate of the thermodynamic T_{BKT} . To estimate the sensitivity to the chosen fitting interval, we start from the manually selected central window indicated by the black open symbols in Fig. 9 and vary the interval by one or two temperature points around the central window [40]. The resulting representative fitting parameters for $q = 0.6$ and isotropic dissipation are summarized in Table II. Unlike the critical-scaling transport-extracted temperatures obtained by

TABLE II. Representative Halperin–Nelson fitting parameters for the normalized linear resistance at $L = 100$, $q = 0.6$, and isotropic dissipation $r_{0,x} = r_{0,y} = 1$. The HN fit uses Eq. (42) over the representative central window shown in Fig. 9, with the fit performed in log space. T_μ^{HN} is reported as the mean over shifted-window variants; parentheses denote the combined uncertainty. The parameters $r_\mu^{\text{HN},0}$, b_μ , and χ_v^2 refer to the central-window fit.

| j | Current direction | T_μ^{HN} | $r_\mu^{\text{HN},0}$ | b_μ | χ_v^2 |
|-------|-------------------|---------------------|-----------------------|---------|------------|
| 0.01 | $j \parallel x$ | 0.483(6) | 2.286 | 1.240 | 1.89 |
| 0.01 | $j \parallel y$ | 0.465(5) | 3.341 | 1.335 | 1.80 |
| 0.005 | $j \parallel x$ | 0.477(5) | 2.450 | 1.316 | 2.17 |
| 0.005 | $j \parallel y$ | 0.458(6) | 4.230 | 1.516 | 4.45 |
| 0.001 | $j \parallel x$ | 0.484(6) | 2.264 | 1.232 | 0.58 |
| 0.001 | $j \parallel y$ | 0.452(6) | 5.300 | 1.688 | 0.71 |

the $\alpha = 3$ and FSS criteria, the HN transport-extracted temperatures show a directional separation, $T_x^{\text{HN}} > T_y^{\text{HN}}$.

The values reported in Table II use the mean of T_μ^{HN} over the shifted-window variants. The quoted uncertainty combines the statistical uncertainty of the central nonlinear fit and the systematic window uncertainty $\sigma_{T_\mu^{\text{HN}}}^{\text{HN}} = \sqrt{(\sigma_{\text{stat},\mu}^{\text{HN}})^2 + (\sigma_{\text{win},\mu}^{\text{HN}})^2}$, where $\sigma_{\text{stat},\mu}^{\text{HN}}$ is the contribution from the central nonlinear fit, and $\sigma_{\text{win},\mu}^{\text{HN}}$ is the standard deviation of T_μ^{HN} over the shifted-window variants. The reduced χ_v^2 in Table II is reported for the central-window log-space fit.

The physical origin of this apparent splitting lies in the distinction between the true asymptotic critical regime and the operational crossover regime. However, in any numerical simulation and indeed in any real experiment, finite system size, finite probe current, and the available linear-response window cut off this divergence and restrict the fit to a higher-temperature crossover regime[41]. Moreover, Ref. [42] shows that finite-size effects and inhomogeneity can broaden the resistive transition, generate resistive tails, and make the physical interpretation of HN fitting parameters nontrivial. In the present clean model, the cutoff is caused by the finite L , finite j , and finite fitting-window constraints of the transport simulation. Consequently, the linear-response $r_{\text{lin}}-T$ data are necessarily truncated, forcing the HN fits to be performed in a slightly higher-temperature crossover regime (as evidenced by $T_\mu^{\text{HN}} > T_{\text{BKT}}$ in all our fits). In this crossover regime, non-universal short-range physics—such as the bare anisotropic Josephson couplings—dominates the shape of the resistive curve. Because these short-range parameters are anisotropic, the resistive curves are reshaped differently along x and y , causing the HN fit to yield two distinct apparent HN transport-extracted temperatures T_μ^{HN} 's even though the thermodynamic transition remains single.

In the combined limit $L \rightarrow \infty$ and $j \rightarrow 0$, the finite-size and finite-current cutoffs are removed and the HN fit can access the asymptotic critical regime. In that limit, both T_x^{HN} and T_y^{HN} are expected to converge to the single thermodynamic T_{BKT} dictated by the geometric-mean stiffness. The directional separation observed at the accessible (L, j) is therefore a finite-size, finite-current feature of the clean anisotropic baseline,

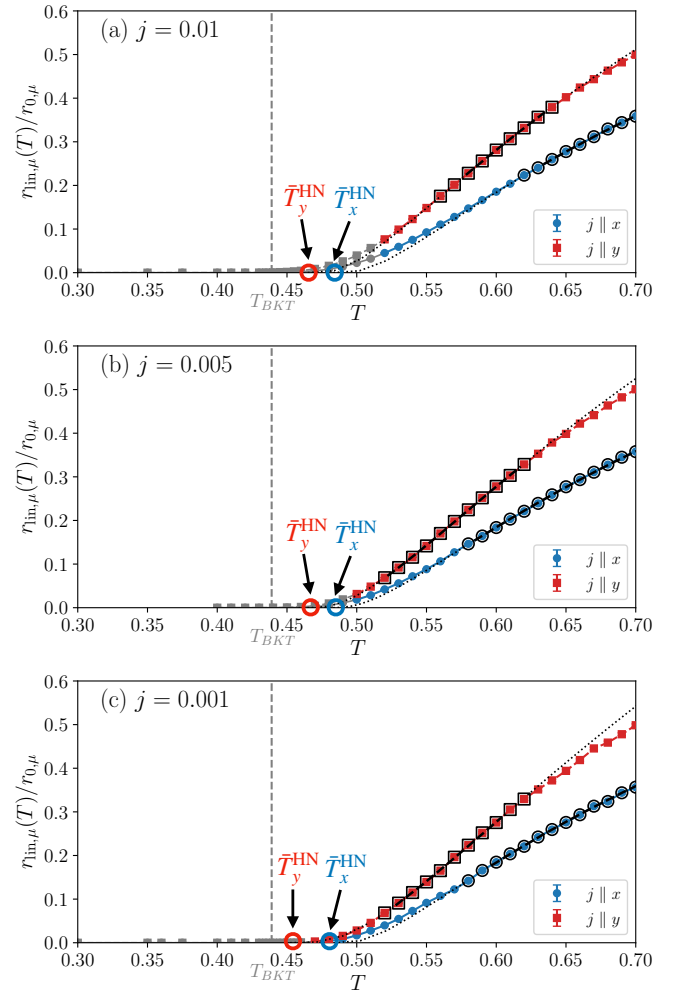


FIG. 9. Halperin–Nelson fits of the normalized linear resistance for $L = 100$, $q = 0.6$, and isotropic dissipation $r_{0,x} = r_{0,y} = 1$ at (a) $j = 0.01$, (b) $j = 0.005$, and (c) $j = 0.001$. Blue circles and red squares denote currents along x and y , respectively. Dashed black curves are fits to Eq. (42) over the representative windows marked by black open symbols. The vertical gray dashed line indicates the equilibrium $T_{\text{BKT}} \approx 0.439$. Gray points lie outside the verified linear-response window and are not used for the HN fitting. The fitted values satisfy $T_x^{\text{HN}} > T_y^{\text{HN}}$ even though the critical-scaling criteria give a single transition temperature.

not a property of the thermodynamic transition.

The $q = 0.6$ example already contains the main distinction. Critical-scaling transport criteria ($\alpha = 3$ and FSS) give a single transport-extracted temperature near 0.44, consistent with the equilibrium BKT temperature. By contrast, curve-shape transport criteria applied to the low-current $r_{\text{lin}}-T$ curves yield direction-dependent transport-extracted temperatures, with the larger $E_{J,\mu}$ direction giving the higher extracted value. Within the present model, these curve-shape transport-extracted temperatures are operational quantities rather than evidence for a split thermodynamic transition.

TABLE III. Dimensionless critical-scaling transport-extracted temperatures obtained from critical-scaling criteria with isotropic shunt resistance $r_{0,x} = r_{0,y} = 1$. The $\alpha = 3$ criterion uses E - j data for $L = 100$, while the dynamic FSS analysis uses $L = 20, 40, 60, 80, 100$ with $z = 2$.

| Criterion | Current direction | $q = 0.5$ | $q = 0.6$ | $q = 0.7$ |
|--------------|-------------------|-----------|-----------|-----------|
| $\alpha = 3$ | $j \parallel x$ | 0.45 | 0.44 | 0.42 |
| $\alpha = 3$ | $j \parallel y$ | 0.45 | 0.44 | 0.42 |
| dynamic FSS | $j \parallel x$ | 0.45 | 0.44 | 0.42 |
| dynamic FSS | $j \parallel y$ | 0.45 | 0.44 | 0.42 |

TABLE IV. Dimensionless curve-shape transport-extracted temperatures obtained from the $r_{\text{lin}}-T$ curves for $L = 100$ with isotropic shunt resistance $r_{0,x} = r_{0,y} = 1$. The HN entries are obtained by fitting Eq. (42) within the verified linear-response window. The 1% criterion means the 1% threshold defined by $r_{\text{lin},\mu}/r_{0,\mu} = 0.01$ and is reported only for $j = 0.001$, for which the threshold crossing lies inside the linear-response window. Parentheses for the HN entries denote the combined uncertainty from the covariance of the central-window nonlinear fit and the standard deviation over shifted fitting windows, and threshold values are direct interpolation read-offs. Dashes for $q = 0.5$ indicate that no reliable threshold temperature is assigned within the verified linear-response window.

| Criterion | j | Current direction | $q = 0.5$ | $q = 0.6$ | $q = 0.7$ |
|-----------|-------|-------------------|-----------|-----------|-----------|
| HN fit | 0.01 | $j \parallel x$ | 0.462(4) | 0.483(6) | 0.456(6) |
| HN fit | 0.01 | $j \parallel y$ | 0.462(4) | 0.465(5) | 0.430(10) |
| HN fit | 0.005 | $j \parallel x$ | 0.461(4) | 0.477(5) | 0.464(9) |
| HN fit | 0.005 | $j \parallel y$ | 0.461(4) | 0.458(6) | 0.434(9) |
| HN fit | 0.001 | $j \parallel x$ | 0.460(6) | 0.484(6) | 0.448(13) |
| HN fit | 0.001 | $j \parallel y$ | 0.460(6) | 0.452(6) | 0.438(11) |
| 1% | 0.001 | $j \parallel x$ | — | 0.492 | 0.472 |
| 1% | 0.001 | $j \parallel y$ | — | 0.484 | 0.456 |

2. Varying the anisotropy parameter q

We now keep the dissipative channel isotropic, $r_{0,x} = r_{0,y} = 1$, and compare $q = 0.6$ with $q = 0.7$ on the same $L = 100$ lattice, using $q = 0.5$ as the isotropic reference. The critical-scaling criteria are collected in Table III, while the curve-shape-based temperatures extracted from the $r_{\text{lin}}-T$ curves are collected in Table IV.

The $\alpha = 3$ and FSS criteria again select a single temperature for each q . By contrast, the stronger splitting at $q = 0.7$ is visible in Fig. 10(c), where the low-resistance threshold is crossed at more clearly separated temperatures than in Fig. 10(b).

$$\left. \frac{T_y^{1\%}}{T_x^{1\%}} \right|_{q=0.6} = 0.984, \quad \left. \frac{T_y^{1\%}}{T_x^{1\%}} \right|_{q=0.7} = 0.966. \quad (43)$$

Within this minimal model, increasing the coupling anisotropy enhances the apparent directional separation extracted from the 1% threshold criterion, while the critical-scaling criteria continue to give a single transition.

TABLE V. Dimensionless transport temperatures extracted from critical-scaling criteria with anisotropic shunt resistance $r_{0,x} = 1$ and $r_{0,y} = 1/2$. The $\alpha = 3$ criterion uses E - j data for $L = 100$, while the dynamic FSS analysis uses $L = 20, 40, 60, 80, 100$ with $z = 2$.

| Criterion | Current direction | $q = 0.5$ | $q = 0.6$ | $q = 0.7$ |
|--------------|-------------------|-----------|-----------|-----------|
| $\alpha = 3$ | $j \parallel x$ | 0.45 | 0.44 | 0.42 |
| $\alpha = 3$ | $j \parallel y$ | 0.45 | 0.44 | 0.42 |
| dynamic FSS | $j \parallel x$ | 0.45 | 0.44 | 0.42 |
| dynamic FSS | $j \parallel y$ | 0.45 | 0.44 | 0.42 |

3. Turning on anisotropy in the dissipative channel

We next introduce anisotropy in the dissipative channel by setting

$$r_{0,x} = 1, \quad r_{0,y} = \frac{1}{2},$$

and study $q = 0.5, 0.6$, and 0.7 on the same $L = 100$ lattice. Because $r_{0,\mu}$ enters only the RSJD dynamics, based on the analysis in Sec. II B, this change does not modify the equilibrium transition. However, it can further reshape the nonequilibrium transport properties.

While the phase-only model does not explicitly include microscopic single-electron physics (such as Fermi surface anisotropies), the anisotropic shunt resistance $r_{0,\mu}$ phenomenologically captures an anisotropic viscous drag (or mobility) for moving vortices. When a vortex moves across the system, the local phase winding generates a voltage $V \propto \dot{\phi}$, and the energy dissipated is proportional to $V^2/r_{0,\mu}$. Therefore, making $r_{0,x} \neq r_{0,y}$ imposes an anisotropic vortex viscosity: vortices experience more friction moving along one axis than the other, which splits the simulated $r_{\text{lin}}-T$ curves even if the underlying thermodynamic stiffness is perfectly isotropic.

At the level of nonlinear transport scaling, Table V shows that the $\alpha = 3$ and FSS criteria still give the same temperature for $j \parallel x$ and $j \parallel y$ for all three values of q .

For the curve-shape analysis, we use the same normalization convention as above and compare $r_{\text{lin},\mu}/r_{0,\mu}$ between the two current directions. The HN temperatures and the 1% threshold temperatures are summarized in Table VI.

Two observations are worth emphasizing. First, anisotropic dissipation alone is already sufficient to give direction-dependent curve-shape transport-extracted temperatures from $r_{\text{lin}}-T$ curves. This is seen most clearly at $q = 0.5$, where the Josephson couplings are isotropic and the equilibrium model has no directional anisotropy. Nevertheless, Table VI shows that $T_x^{\text{HN}}(j) > T_y^{\text{HN}}(j)$ for all three probe currents, and that $T_x^{1\%} > T_y^{1\%}$ at $j = 0.001$. This indicates that the larger shunt resistance along the x direction leads to a higher extracted temperature from the $r_{\text{lin}}-T$ curves, even though the underlying thermodynamic transition is isotropic. This further supports the conclusion that a directional separation of transport-extracted temperatures does not by itself imply a split equilibrium BKT temperature or thermodynamic transition.

Second, as shown in Fig. 10, anisotropic dissipation can further enhance the apparent splitting extracted from the low-

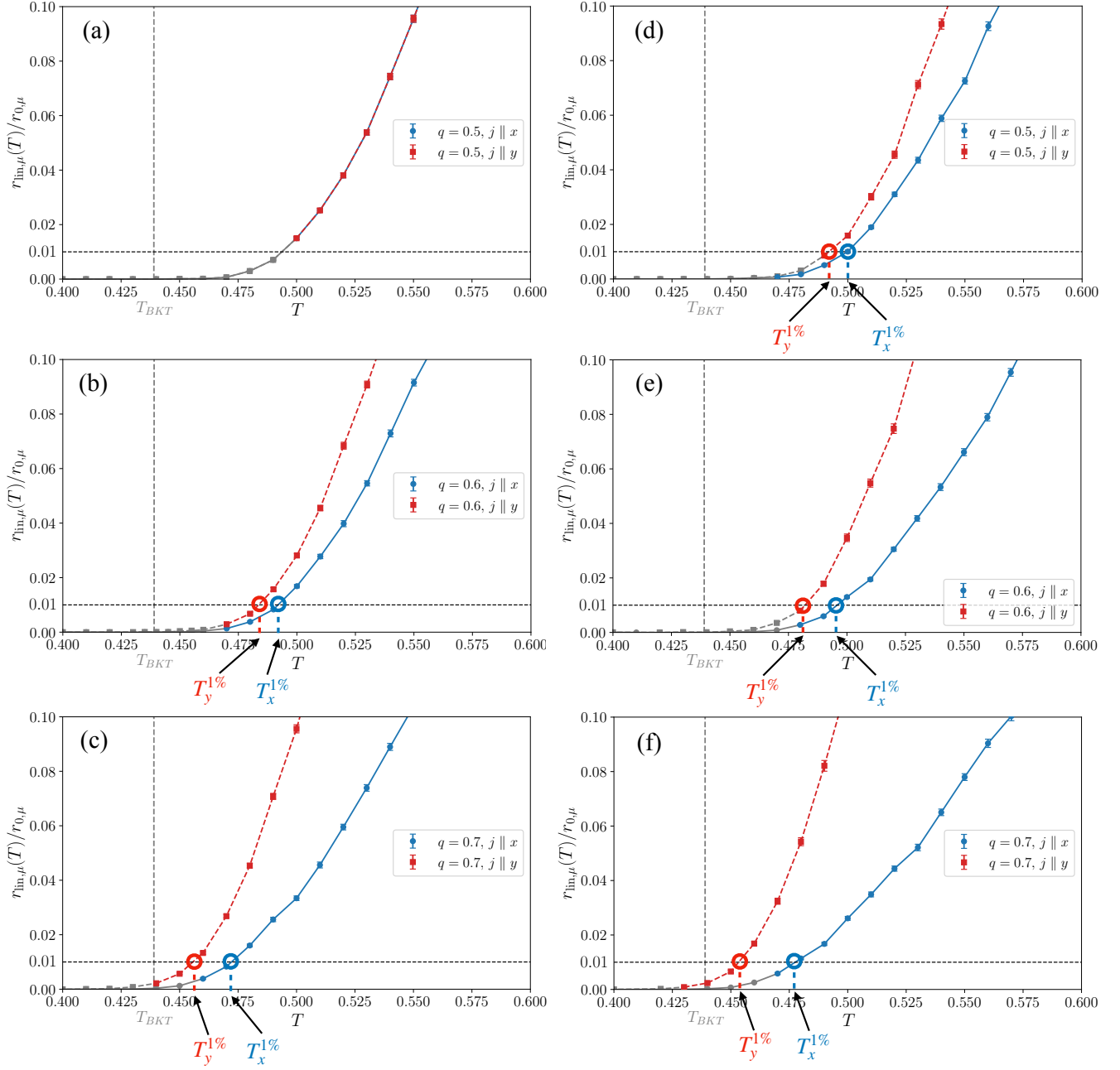


FIG. 10. Effect of coupling and dissipation anisotropy on the low-resistance threshold. All panels show $r_{\text{lim},\mu}(T)/r_{0,\mu}$ versus T for $L = 100$ and $j = 0.001$. The top row, (a)–(c), uses isotropic dissipation $r_{0,x} = r_{0,y} = 1$ for $q = 0.5, 0.6, 0.7$. The bottom row, (d)–(f), uses anisotropic dissipation $r_{0,x} = 1, r_{0,y} = 1/2$ for the same values of q . The horizontal dashed line marks the 1% threshold $r_{\text{lim},\mu}/r_{0,\mu} = 0.01$, and the vertical dashed line marks the corresponding equilibrium T_{BKT} . For $q = 0.5$ with isotropic dissipation (panel (a)), no reliable threshold temperature is assigned within the verified linear-response window. However, with anisotropic dissipation (panel (d)), the 1% threshold is crossed at different temperatures for the two directions, even though the underlying thermodynamic transition is isotropic. For $q = 0.6$ and $q = 0.7$ (panel (b), (c), (e) and (f)), assigning the larger shunt resistance to the more strongly coupled direction enhances the apparent threshold splitting, while the thermodynamic transition remains single.

resistance threshold criterion when the larger shunt resistance is assigned to the more strongly coupled direction. For the 1%

threshold at $j = 0.001$, we find

$$\left. \frac{T_y^{1\%}}{T_x^{1\%}} \right|_{q=0.6} = 0.972, \quad \left. \frac{T_y^{1\%}}{T_x^{1\%}} \right|_{q=0.7} = 0.948. \quad (44)$$

These ratios are smaller than those in Eq. (43), meaning

TABLE VI. Dimensionless transport temperatures extracted from the $r_{\text{in}}-T$ curves for $L = 100$ with anisotropic shunt resistance $r_{0,x} = 1$ and $r_{0,y} = 1/2$. The HN entries are obtained by fitting Eq. (42) within the verified linear-response window. The 1% threshold is defined by $r_{\text{in},\mu}/r_{0,\mu} = 0.01$. Parentheses for the HN entries denote the combined uncertainty from the covariance of the central-window nonlinear fit and the standard deviation over shifted fitting windows, and threshold values are direct interpolation read-offs.

| Criterion | j | Current direction | $q = 0.5$ | $q = 0.6$ | $q = 0.7$ |
|-----------|-------|-------------------|-----------|-----------|-----------|
| HN fit | 0.01 | $j \parallel x$ | 0.492(4) | 0.477(3) | 0.444(5) |
| HN fit | 0.01 | $j \parallel y$ | 0.473(4) | 0.473(6) | 0.429(7) |
| HN fit | 0.005 | $j \parallel x$ | 0.484(3) | 0.470(3) | 0.445(4) |
| HN fit | 0.005 | $j \parallel y$ | 0.464(4) | 0.463(5) | 0.434(10) |
| HN fit | 0.001 | $j \parallel x$ | 0.488(4) | 0.472(8) | 0.443(15) |
| HN fit | 0.001 | $j \parallel y$ | 0.469(6) | 0.468(6) | 0.426(12) |
| 1% | 0.001 | $j \parallel x$ | 0.500 | 0.496 | 0.478 |
| 1% | 0.001 | $j \parallel y$ | 0.492 | 0.482 | 0.453 |

that the corresponding directional separation is enhanced by anisotropic dissipation. Equivalently, the relative splitting $1 - T_y^{1\%}/T_x^{1\%}$ increases from 1.6% to 2.8% for $q = 0.6$, and from 3.4% to 5.2% for $q = 0.7$. On the other hand, the critical-scaling criteria continue to yield a single extracted temperature.

IV. SUMMARY AND DISCUSSION

In this work, we have established a clean theoretical baseline for the transport phenomenology of anisotropic two-dimensional superconductors. By studying a minimal anisotropic JJA model in both equilibrium and nonequilibrium, we demonstrated that a system with a single thermodynamic BKT transition can nonetheless exhibit direction-dependent transport-extracted temperatures in operational transport metrics. This provides a minimal route to an apparent “double- T_c ” without splitting the thermodynamic transition.

Within this minimal model, the apparent double- T_c has a clear physical origin: anisotropic phase stiffness and anisotropic dissipation (vortex viscosity) naturally reshape the $r_{\text{in}}-T$ curves differently for different current directions. Because finite system sizes and finite measurement currents cut off the critical divergence of the correlation length, experimental and numerical fits are forced into a higher-temperature crossover regime. In this regime, standard curve-shape criteria—such as fixed-resistance thresholds or Halperin–Nelson fits—inherently inherit this anisotropy, producing a spurious splitting of the curve-shape transport-extracted temperatures.

Crucially, we found a stark contrast between curve-shape criteria and critical scaling criteria. Dynamic finite-size scaling and the $\alpha = 3$ exponent in the simulated $E-j$ characteristics, equivalently the $I-V$ exponent in experimental notation, inherently account for finite-size cutoffs and are tied to the universal stiffness jump. Consequently, within the numerical resolution of the simulations, these criteria are much less sensitive to the crossover anisotropy and remain consistent with

the single equilibrium T_{BKT} .

This contrast serves as a useful diagnostic comparison for experiments. In our clean, minimal model, trivial anisotropy yields an apparent $R-T$ splitting of roughly 5% (e.g., $T_y^{1\%}/T_x^{1\%} \approx 0.948$ for $q = 0.7$ with anisotropic dissipation), while maintaining a unified $\alpha = 3$ crossing. This comparison also clarifies the scope of our baseline model. Recent experiments on $\text{EuO}/\text{KTaO}_3(111)$ interfaces [11] report a much larger T_c splitting ($\sim 20\%$) that persists even in the $\alpha = 3$ criterion. Such behavior is not reproduced by the clean anisotropic phase-only model studied here. It therefore points to physics beyond this minimal baseline, although the present work alone does not determine the microscopic origin of that physics. Possible ingredients include, for example, fractional or half-vortices, directed pinning or disorder, intrinsic normal-state anisotropy, multiorbital effects, magnetic proximity effects, or stripe-like spatial textures [10–13].

Ultimately, before invoking exotic physics, apparent splittings extracted only from $R-T$ curve-shape criteria should first be tested against anisotropic crossover effects. By systematically comparing curve-shape criteria from $R-T$ curves with critical-scaling criteria from nonlinear $I-V$ characteristics, experimentalists can cleanly distinguish trivial transport artifacts from genuinely new superconducting phases of matter.

ACKNOWLEDGMENTS

This work is supported by the National Key R&D Program of China (Grant No. 2022YFA1403201) and the National Natural Science Foundation of China (Grant No. 12074411). We thank Ziji Xiang, Zi-Xiang Li, Kun Jiang, Hong Yao, Gaurav Khairnar and Zhipeng Xu for helpful discussions.

DATA AVAILABILITY

The data that support the findings of this article are available from the authors upon reasonable request.

Appendix A: The Directional Helicity Modulus

1. Derivation of Equation (17)

Starting from Eq. (14), we fix the direction of the extra twist to be $\nu = x, y$ and write the free energy as

$$F = -T \ln Z, \quad Z = \int \mathcal{D}\theta \exp[-\beta H(\theta, \Phi_\nu)],$$

where $H(\theta, \Phi_\nu)$ incorporates a uniform twist per bond $\delta_\nu \equiv \Phi_\nu/L$ only on bonds parallel to the chosen direction ν :

$$H(\theta, \Phi_\nu) = - \sum_i \sum_{\mu=x,y} E_{J\mu} \cos(\theta_{i+\hat{\mu}} - \theta_i + \delta_\nu \delta_{i\nu}). \quad (\text{A1})$$

The first derivative of the free energy with respect to δ_ν is

$$\frac{\partial F}{\partial \delta_\nu} = -T \frac{1}{Z} \frac{\partial Z}{\partial \delta_\nu} = \left\langle \frac{\partial H}{\partial \delta_\nu} \right\rangle,$$

where

$$\frac{\partial H}{\partial \delta_\nu} = \sum_i E_{J,\nu} \sin(\theta_{i+\hat{\nu}} - \theta_i + \delta_\nu). \quad (\text{A2})$$

The second derivative is

$$\frac{\partial^2 F}{\partial \delta_\nu^2} = \left\langle \frac{\partial^2 H}{\partial \delta_\nu^2} \right\rangle - \beta \left[\left\langle \left(\frac{\partial H}{\partial \delta_\nu} \right)^2 \right\rangle - \left\langle \frac{\partial H}{\partial \delta_\nu} \right\rangle^2 \right].$$

The second derivative of the Hamiltonian is

$$\frac{\partial^2 H}{\partial \delta_\nu^2} = \sum_i E_{J,\nu} \cos(\theta_{i+\hat{\nu}} - \theta_i + \delta_\nu). \quad (\text{A3})$$

Evaluating these expressions at $\delta_\nu = 0$ and then relabeling $\nu \rightarrow \mu$ gives Eq. (17):

$$\Upsilon_\mu(L, T) = \frac{1}{L^2} \left. \frac{\partial^2 F}{\partial \delta_\mu^2} \right|_{\delta_\mu=0} = \frac{1}{L^2} \langle C_\mu \rangle - \frac{\beta}{L^2} [\langle S_\mu^2 \rangle - \langle S_\mu \rangle^2].$$

2. Remark on finite boundary twists

The helicity modulus in the main text (Eq. (14)) is defined at zero boundary twist and is the quantity that enters the equilibrium BKT criterion, Eq. (13).

For a *finite* boundary twist $\Theta_\mu = A_\mu L \neq 0$, one can define two similar objects:

1. the phase stiffness defined in Ref. [43] from the free-energy difference,

$$\Upsilon_\mu^{(1)}(L, T; \Theta_\mu) \equiv \frac{2[F(\Theta_\mu) - F(0)]}{\Theta_\mu^2}, \quad (\text{A4})$$

2. the second derivative of the free energy at a nonzero boundary twist,

$$\Upsilon_\mu^{(2)}(L, T; \Theta_\mu) \equiv \frac{1}{L^2} \left. \frac{\partial^2 F(\Theta_\mu + L\delta_\mu)}{\partial \delta_\mu^2} \right|_{\delta_\mu=0}, \quad (\text{A5})$$

which also admits an expression analogous to Eq. (17) but with averages taken in the finite-twisted ensemble.

These need not coincide with the standard Υ_μ defined under zero boundary twist. Indeed, Ref. [43] demonstrated that in the two-dimensional XY model $\Upsilon^{(1)}$ (denoted there as $\rho_s(\Theta)$) deviates from the helicity modulus defined under zero boundary twist when Θ_μ is finite, owing to the mixing of states with opposite chirality. The same logic implies that $\Upsilon_\mu^{(2)}$ evaluated at a finite background twist should not be regarded as the standard helicity modulus.

For the present problem, the reason finite twists cannot split the thermodynamic BKT transition is straightforward. When the total twist Θ_μ is held fixed while $L \rightarrow \infty$, the corresponding gauge field scales as $A_\mu = \Theta_\mu/L \rightarrow 0$. At the spin-wave level we have

$$\frac{\Delta F_{\text{sw}}}{L^2} \simeq \frac{1}{2} \Upsilon_\mu(\Theta_\mu/L)^2 = \mathcal{O}(L^{-2}). \quad (\text{A6})$$

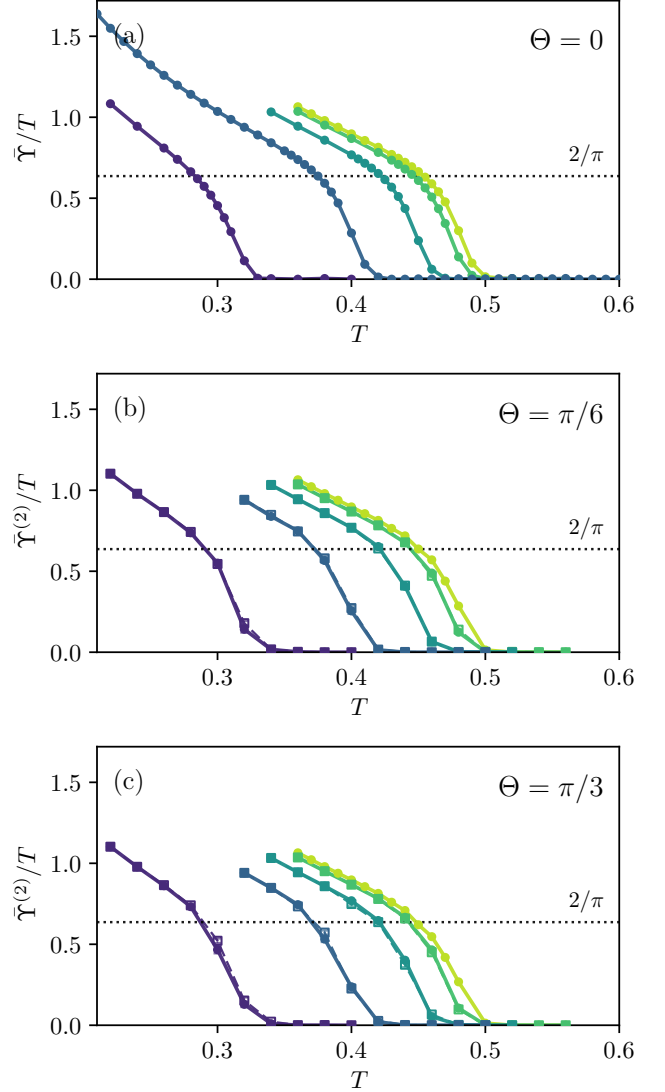
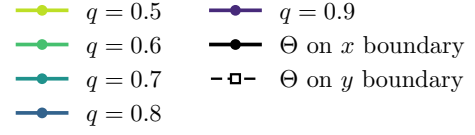


FIG. 11. Geometric-mean stiffness response divided by temperature with system size $L = 200$ and boundary twists: (a) $\Theta = 0$, (b) $\Theta = \pi/6$, and (c) $\Theta = \pi/3$. For finite twist panels (b) and (c), we evaluate $\tilde{\Upsilon}^{(2)} = \sqrt{\Upsilon_x^{(2)} \Upsilon_y^{(2)}}$ with $\Upsilon_\mu^{(2)}$ defined by Eq. (A5). The solid circles and open squares in (b) and (c) correspond to $(\Theta_x, \Theta_y) = (\Theta, 0)$ and $(0, \Theta)$. The dashed line indicates $2/\pi$.

Thus a finite boundary twist modifies only boundary and finite-size contributions, leaving the bulk long-wavelength theory unchanged. The renormalization-group flow therefore remains governed by a single geometric-mean stiffness.

As a consistency check, we have evaluated $\tilde{\Upsilon}^{(2)}$ at $(\Theta_x, \Theta_y) = (\pi/6, 0), (0, \pi/6), (\pi/3, 0), (0, \pi/3)$ for $q = 0.5, 0.6, 0.7, 0.8, 0.9$ up to $L = 200$ by Monte Carlo simula-

tions. Ref. [43] has pointed out that under a finite twist, the standard Wolff cluster update is no longer appropriate and one may employ Metropolis sweeps[44, 45]. This stems from the fact that when the boundary twist is finite, the bond energy is not preserved under the cluster flip

$$\theta_i \mapsto \theta_i^* = 2\alpha - \theta_i,$$

where α is the random angle and θ_i is in the cluster. However, we can use a modified cluster update:

$$\theta_i \mapsto \theta_i^* = \theta_i + \pi. \quad (\text{A7})$$

Unlike the standard reflection update, this “ π -shift” leaves the gauge-invariant phase difference of every internal cluster bond unchanged, even in the presence of a finite background twist. The remaining boundary bonds are treated by the usual Wolff-type acceptance construction, so that detailed balance is maintained. However, the shift changes phases only by π and is not ergodic by itself. We consequently combine it with Metropolis sweeps, which restore ergodicity while retaining the acceleration from the cluster algorithm.

As shown in Fig. 11, within numerical resolution, these finite-twist checks show only a single crossing with $2/\pi$ for each tested anisotropy. Moreover, in Figs. 11(b) and 11(c), applying the same total boundary twist along x direction $(\Theta_x, \Theta_y) = (\Theta, 0)$ and y direction $(\Theta_x, \Theta_y) = (0, \Theta)$ results in nearly overlapping curves. This indicates that the finite-twist response does not show a robust direction-dependent splitting. Therefore, finite boundary twists do not generate a second thermodynamic transition in our anisotropic model.

Appendix B: The RSJD equations under FTBC

The total current $I_{i,\mu}$ on the bond connecting site i to $i + \hat{\mu}$ is given by Eq. (22). Current conservation at each site requires

$$\sum_{\mu=x,y} (I_{i,\mu} - I_{i-\hat{\mu},\mu}) = 0. \quad (\text{B1})$$

Following the FTBC formulation [15, 28], the spatially averaged current must match the external applied current density $I_{\text{ext},\mu}^{\text{phys}}$,

$$\frac{1}{L^2} \sum_i I_{i,\mu} = I_{\text{ext},\mu}^{\text{phys}}, \quad \mu = x, y. \quad (\text{B2})$$

To make the equations dimensionless, we introduce a reference energy scale E_* and a reference resistance R_* , and define the scales for current, time, and temperature as:

$$I_* \equiv \frac{2e}{\hbar} E_*, \quad \tau_* \equiv \frac{\hbar}{2eI_*R_*}, \quad T_* \equiv \frac{E_*}{k_B}. \quad (\text{B3})$$

Dimensionless variables are then defined by

$$\tau \equiv \frac{t}{\tau_*}, \quad j_\mu \equiv \frac{I_{\text{ext},\mu}^{\text{phys}}}{I_*}. \quad (\text{B4})$$

The dimensionless total bond current is $\mathcal{J}_{i,\mu} = I_{i,\mu}/I_*$. Using the dimensionless parameters J_μ and $r_{0,\mu}$ defined in the main text, $\mathcal{J}_{i,\mu}$ becomes

$$\mathcal{J}_{i,\mu} = J_\mu \sin \phi_{i,\mu} + \frac{1}{r_{0,\mu}} \dot{\phi}_{i,\mu} + \zeta_{i,\mu}, \quad (\text{B5})$$

where $\zeta_{i,\mu} = \eta_{i,\mu}/I_*$ is the dimensionless noise. The phase difference is $\phi_{i,\mu} = \theta_{i+\hat{\mu}} - \theta_i - \Delta_\mu$, so $\dot{\phi}_{i,\mu} = \dot{\theta}_{i+\hat{\mu}} - \dot{\theta}_i - \dot{\Delta}_\mu$.

Substituting $\mathcal{J}_{i,\mu}$ into the dimensionless form of Eq. (B1) gives

$$-\sum_{\mu=x,y} \frac{1}{r_{0,\mu}} (\dot{\theta}_{i+\hat{\mu}} - 2\dot{\theta}_i + \dot{\theta}_{i-\hat{\mu}}) = S_i, \quad (\text{B6})$$

where the source term is

$$S_i = \sum_{\mu=x,y} [\mathcal{J}_{i,\mu}^{\text{sc}} - \mathcal{J}_{i-\hat{\mu},\mu}^{\text{sc}} + \zeta_{i,\mu} - \zeta_{i-\hat{\mu},\mu}]. \quad (\text{B7})$$

The terms proportional to $\dot{\Delta}_\mu$ cancel out in the site current conservation because they are spatially uniform. Equation (B6) can be inverted using the weighted Laplacian operator

$$D_{ij}^{(r_0)} = \sum_{\mu} \frac{1}{r_{0,\mu}} (\delta_{j,i+\hat{\mu}} - 2\delta_{j,i} + \delta_{j,i-\hat{\mu}})$$

and the Green’s function of $-D^{(r_0)}$,

$$\sum_k [-D^{(r_0)}]_{ik} G_{kj}^{(r_0)} = \delta_{ij} - \frac{1}{L^2}.$$

With this convention, $-D^{(r_0)}\dot{\theta} = S$ gives $\dot{\theta}_i = \sum_j G_{ij}^{(r_0)} S_j$, which yields Eq. (27). Since $\sum_i S_i = 0$, the uniform mode $\sum_i \dot{\theta}_i$ is decoupled and we can set it to zero.

To obtain the equation for the twist variables Δ_μ , we substitute $\mathcal{J}_{i,\mu}$ into the dimensionless form of Eq. (B2):

$$\frac{1}{L^2} \sum_i \left[\mathcal{J}_{i,\mu}^{\text{sc}} + \frac{1}{r_{0,\mu}} (\dot{\theta}_{i+\hat{\mu}} - \dot{\theta}_i - \dot{\Delta}_\mu) + \zeta_{i,\mu} \right] = j_\mu.$$

Under periodic boundary conditions for θ_i , the sum $\sum_i (\dot{\theta}_{i+\hat{\mu}} - \dot{\theta}_i)$ vanishes. Solving for $\dot{\Delta}_\mu$ then directly yields Eq. (28).

[1] V. L. Berezinskii, Sov. Phys. JETP **32**, 493 (1971).

[2] J. M. Kosterlitz and D. J. Thouless, *Journal of Physics C: Solid*

- State Physics **6**, 1181 (1973).
- [3] J. M. Kosterlitz, *Journal of Physics C: Solid State Physics* **7**, 1046 (1974).
- [4] D. R. Nelson and J. M. Kosterlitz, *Phys. Rev. Lett.* **39**, 1201 (1977).
- [5] M. E. Fisher, M. N. Barber, and D. Jasnow, *Phys. Rev. A* **8**, 1111 (1973).
- [6] P. Minnhagen, *Rev. Mod. Phys.* **59**, 1001 (1987).
- [7] V. Ambegaokar, B. I. Halperin, D. R. Nelson, and E. D. Siggia, *Phys. Rev. Lett.* **40**, 783 (1978).
- [8] V. Ambegaokar, B. I. Halperin, D. R. Nelson, and E. D. Siggia, *Phys. Rev. B* **21**, 1806 (1980).
- [9] B. I. Halperin and D. R. Nelson, *J. Low Temp. Phys.* **36**, 599 (1979).
- [10] X. Hua, Z. Zeng, F. Meng, H. Yao, Z. Huang, X. Long, Z. Li, Y. Wang, Z. Wang, T. Wu, Z. Weng, Y. Wang, Z. Liu, Z. Xiang, and X. Chen, *Nature Physics* **20**, 957 (2024).
- [11] Z. Huang, Z. Wang, X. Hua, H. Wang, Z. Li, S. Liu, Z. Wang, F. Quan, Z. Wang, J. Tao, J. J. He, Z. Xiang, and X. Chen, *Directional-dependent Berezinskii-Kosterlitz-Thouless transition at EuO/KTaO₃(111) interfaces* (2026), arXiv:2604.00608 [cond-mat.supr-con].
- [12] Z.-X. Li, S. A. Kivelson, and D.-H. Lee, *Theory of an infinitely anisotropic phase of a two-dimensional superconductor* (2024), arXiv:2407.10269 [cond-mat.supr-con].
- [13] Z. Xu, K. Jiang, and J. Hu, *Anisotropic vortex motion and two-dimensional superconducting transition* (2025), arXiv:2506.05830 [cond-mat.supr-con].
- [14] K. K. Mon and S. Teitel, *Phys. Rev. Lett.* **62**, 673 (1989).
- [15] J. S. Chung, K. H. Lee, and D. Stroud, *Phys. Rev. B* **40**, 6570 (1989).
- [16] B. J. Kim, P. Minnhagen, and P. Olsson, *Phys. Rev. B* **59**, 11506 (1999).
- [17] M. Y. Choi, G. S. Jeon, and M. Yoon, *Phys. Rev. B* **62**, 5357 (2000).
- [18] K. Medvedyeva, B. J. Kim, and P. Minnhagen, *Phys. Rev. B* **62**, 14531 (2000).
- [19] P. Olsson, *Phys. Rev. B* **52**, 4511 (1995).
- [20] P. Olsson, *Phys. Rev. B* **52**, 4526 (1995).
- [21] H. Weber and P. Minnhagen, *Phys. Rev. B* **37**, 5986 (1988).
- [22] D. M. Hübscher and S. Wessel, *Phys. Rev. E* **87**, 062112 (2013).
- [23] M. R. Beasley, J. E. Mooij, and T. P. Orlando, *Phys. Rev. Lett.* **42**, 1165 (1979).
- [24] T. Ohta and D. Jasnow, *Phys. Rev. B* **20**, 139 (1979).
- [25] S. Teitel and C. Jayaprakash, *Phys. Rev. B* **27**, 598 (1983).
- [26] J. V. José, L. P. Kadanoff, S. Kirkpatrick, and D. R. Nelson, *Phys. Rev. B* **16**, 1217 (1977).
- [27] N. Schultka and E. Manousakis, *Phys. Rev. B* **49**, 12071 (1994).
- [28] C. J. Lobb, D. W. Abraham, and M. Tinkham, *Phys. Rev. B* **27**, 150 (1983).
- [29] W. C. Stewart, *Applied Physics Letters* **12**, 277 (1968).
- [30] D. E. McCumber, *Journal of Applied Physics* **39**, 3113 (1968).
- [31] A. A. Golubov, M. Y. Kupriyanov, and E. Il'ichev, *Rev. Mod. Phys.* **76**, 411 (2004).
- [32] V. Ambegaokar and B. I. Halperin, *Phys. Rev. Lett.* **22**, 1364 (1969).
- [33] U. Wolff, *Phys. Rev. Lett.* **62**, 361 (1989).
- [34] E. Helfand, *Bell System Technical Journal* **58**, 2289 (1979).
- [35] H. S. Greenside and E. Helfand, *Bell System Technical Journal* **60**, 1927 (1981).
- [36] D. S. Fisher, M. P. A. Fisher, and D. A. Huse, *Phys. Rev. B* **43**, 130 (1991).
- [37] K. Medvedyeva, B. J. Kim, and P. Minnhagen, *Physica C: Superconductivity* **355**, 6 (2001).
- [38] P. C. Hohenberg and B. I. Halperin, *Rev. Mod. Phys.* **49**, 435 (1977).
- [39] Using a narrower tolerance gives fewer accepted data points near the low-resistance side of the transition, whereas a broader tolerance gives a larger operational window. The qualitative comparison between the two current directions is based on the anisotropic shape of the underlying transport curves, rather than the special value of this tolerance.
- [40] If the central window contains the temperature interval $[T_{\text{left}}, T_{\text{right}}]$, we generate shifted windows by moving the left and right endpoints independently by $0, \pm 1, \pm 2$ temperature-grid points, while retaining only successful fits with positive resistance data and with all points inside the linear-response regime. This procedure gives up to 25 window variants for each current direction.
- [41] M. V. Simkin and J. M. Kosterlitz, *Phys. Rev. B* **55**, 11646 (1997).
- [42] L. Benfatto, C. Castellani, and T. Giamarchi, *Phys. Rev. B* **80**, 214506 (2009).
- [43] G. Khairnar and T. Vojta, *Phys. Rev. E* **111**, 024114 (2025).
- [44] N. Metropolis and S. Ulam, *Journal of the American Statistical Association* **44**, 335 (1949), PMID: 18139350.
- [45] N. Metropolis, A. W. Rosenbluth, M. N. Rosenbluth, A. H. Teller, and E. Teller, *The Journal of Chemical Physics* **21**, 1087 (1953).